Multirate Spectral Domain Optical Coherence Tomography

Prabhav Gaur , Andrew Grieco, and Yeshaiahu Fainman

Abstract—Optical coherence tomography is state-of-the-art in non-invasive imaging of biological structures. Spectral Domain Optical Coherence Tomography is the popularly used variation of this technique, but its performance is limited by the bandwidth and resolution of the system. In this work, we theoretically formulate the use of phase modulators and delay lines to act as filters on the tomography system and scan multiple channels. Various channels are then combined in a digital computer using filter bank theory to improve the sampling rate. The combination of multiple channels allows for increasing the axial resolution and maximum unambiguous range beyond the Nyquist limit. We then simulate the multirate spectral domain optical coherence tomography with 2 channels. We show that a single delay line can improve the axial resolution while a pair of phase modulators can improve the maximum unambiguous range of the system. We also show the use of multirate filter banks to carry out this process. Thus, by using a few extra components in the spectral domain optical coherence tomography, its performance can be increased manifold depending on the number of channels used. The extra cost is the time taken to perform the extra scans that is trivial for stationary objects like biological tissues.

Index Terms—Optical coherence tomography, filter bank.

I. INTRODUCTION

PTICAL Coherence Tomography (OCT) is an important and powerful 3D imaging tool for several biomedical applications. The first OCT was demonstrated three decades ago by [1], but has evolved since then and has remained a major technique to study layered structures for ophthalmology. OCT was initially performed as Time Domain OCT (TD-OCT) [2] which is analogous to ultrasound. TD-OCT uses an echo time delay of backscattered light to create a cross-sectional image of the tissue under investigation. With the improvement in hardware technology, TD-OCT led to Fourier Domain OCT (FD-OCT) [3] which relies on multiple wavelengths to make the axial scan, also called

Manuscript received 15 August 2023; accepted 6 September 2023. Date of publication 11 September 2023; date of current version 20 September 2023. This work was supported in part by the National Science Foundation under Grant ECCS-2023730, in part by the NSF National Nanotechnology Coordinated Infrastructure through San Diego Nanotechnology Infrastructure under Grant ECCS-2025752, and in part by the ASML/Cymer Corporation. (Corresponding author: Prabhav Gaur.)

Prabhav Gaur and Yeshaiahu Fainman are with the Department of Electrical and Computer Engineering, University of California San Diego, La Jolla, CA 92093 USA (e-mail: pgaur@eng.ucsd.edu).

Andrew Grieco is with the Qualcomm Institute, University of California San Diego, La Jolla, CA 92093 USA.

All the simulation in this work has been performed on MATLAB. The code can be found on GitHub repository https://github.com/pgaur7/Multirate_SD_OCT This article has supplementary downloadable material available at https://doi.org/10.1109/JPHOT.2023.3313521, provided by the authors.

Digital Object Identifier 10.1109/JPHOT.2023.3313521

the A-scan. The FD-OCT can be implemented in two different ways, namely Spectral Domain OCT (SD-OCT) [4] and Swept Source OCT (SS-OCT) [5]. Both of them use interferometry of reflected and reference light wave, and measurement of several wavelengths to gather depth information. SD-OCT works with a partially coherent broadband source and a spectrometer is used to detect the interference of different wavelengths. SS-OCT utilizes a wavelength sweep from a coherent laser and the interference is detected using a photodetector. The Fourier transform of the detected signal yields the depth information in both of the above cases. The A-scan can measure up to a depth of few mm with a resolution of few μ m [6], [7]. Multiple A-scan while moving in the other two dimensions, also called B-scan, can be used to determine the 3D structure of the object.

SD-OCT is currently one of the most popular commercial techniques [8] to evaluate tissue structure due to its high data acquisition rate, high axial resolution, good SNR and the simplicity of the hardware required to perform A-scan. SD-OCT has most extensively been used to diagnose diseases and disorders in the brain [9] and retina [10], [11], [12] but has also found application for other tissues such as the breast [13], kidney [14], [15], and skin [16]. Recently, a wide variety of modifications have been applied to SD-OCT to improve its performance [17], [18], [19], [20], [21], [22], [23], [24], [25], [26], [27], [28], [29], [30]. Given enough Signal-to-Noise ratio [31] in the SD-OCT system, the axial resolution and the maximum unambiguous range are determined by the Nyquist-Shannon sampling theorem [32], where frequency and time (length) domain form a fourier pair. Let f_0 be the resolution of the spectrometer being used and B be the bandwidth of the system either limited by source or spectrometer. The axial resolution l_o and maximum unambiguous distance L can be given by

$$l_o = c/B; L = c/2f_o \tag{1}$$

where c is the speed of light in vacuum. Thus, the system after detection behaves like an analog system before and then like a digital system after photodetection.

In this work, we theoretically formulate the use of delay line and phase modulators along with multiple A-scan at the same position to improve the resolution and maximum unambiguous depth of SD-OCT. We show that the use of optical components at various positions in an SD-OCT system can be treated as filters acting on the depth information. By making several scans with different filters, multiple channels can be created that have depth information encoded in them. After detection, the theory of multirate filter banks [33] is used to combine the channels

and increase the resolution in the frequency or length domain. We then simulate simple cases of this system to demonstrate the multirate SD-OCT. This work is based on the principles of linear digital signal processing and statistical optics, which although well known, have not been combined in such a way to improve SD-OCT to the best of our knowledge.

II. FORMULATION

The Multirate filter banks are sets of filters, decimators, and interpolators used widely in conventional digital systems [34]. Usually, decimators downsample the signal after passing through analysis filters. This compressed information is stored or transmitted via a channel. On the other end of the channel, the signal is interpolated or upsampled and passed through synthesis filters to retrieve the original information. The downsampling process means decreasing the system's resolution, which is similar to an undersampled tomography system. The tomography systems are also discrete after detection, and analog filters can be implemented by phase modulation/delay line on the optical carrier signal before detection and by digital processing after detection. Hence, the imaging system can be considered as a multirate filter bank with each scanning cycle representing a single channel and carrying object information in a compressed form. In this work, we formulate the underlying equations governing the SD-OCT to determine the analog filter applied to it. We use the theory of multirate filter bank to determine the digital filters needed to combine back the information. For proof of concept, we simulate a 2-channel filter bank implementation that results in a twofold improvement in both the length and frequency resolution of the tomography system. In our previous work [35], we have demonstrated theoretically and experimentally a similar multirate system for SS-OCT. For SS-OCT, a single phase modulator is sufficient to improve the frequency and length resolution. In this work we simulate a similar result for SD-OCT, where an extra phase modulator and delay line is needed. Also, the formulation requires the inclusion of the statistics of broadband source, which is not necessary for SS-OCT.

A. Spectral Domain OCT

In this section, we formulate the working of a standard SD-OCT for a single A-scan. We consider the statistics of a broadband source and how the autocorrelation function is related to its power spectral density. We then derive the spectrum measured in an SD-OCT device which depends on the spectrum of the broadband source used and the object that is under investigation. Finally, we show that the fourier transform of the measured spectrum gives the depth information of the object.

SD-OCT uses a broadband source for illumination as shown in Fig. 1(a). Let $r_s(t)$ be the complex field emitted by this source as a function of time t. We assume that $r_s(t)$ is an ergodic process, and thus by Wiener-Khinchin theorem [36] the power spectral density S(t) of this source can be given by

$$PSD_s(f) = \mathbb{F}\left\{R_s(\tau)\right\}(f) = S(f) \tag{2}$$

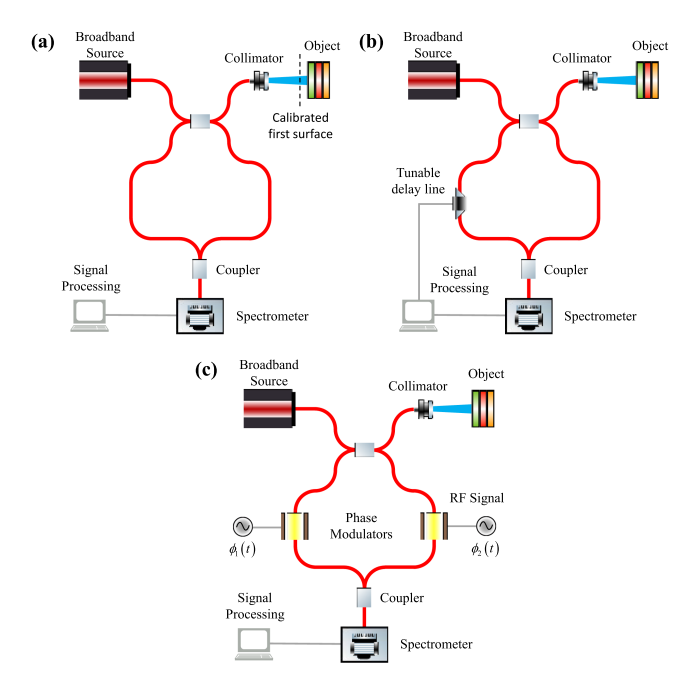


Fig. 1. Setup for SD-OCT along with the variants studied in this work. (a) Regular SD-OCT setup in fiber and the object that is under investigation. (b) Addition of a delay line to SD-OCT in the sample arm. This implements a transfer function in the frequency domain and improves resolution in the length domain. (c) Addition of a couple of phase modulators to sample and reference arms. This implements a transfer function in the length domain and improves the maximum unambiguous range.

where $\mathbb{F}\{.\}$ represents the Fourier transform, f is the frequency and $R_s(\tau)$ is the autocorrelation function of the complex field emitted by the source given by

$$R_{s}(f) = \lim_{T \to \infty} \frac{1}{T} \int_{t=-T/2}^{T/2} r_{s}(t+\tau) r_{s}^{*}(t) dt \qquad (3)$$

Next, consider a heterogeneous object with multiple optical media and their corresponding surface present only at spacings of effective optical distance il_0 from the first surface (Fig. 1(a)). Since a reflected beam will pass through each section twice (once in the transmission direction, and once in the reflected direction), the effective optical path length of each section is defined as twice the distance multiplied by the effective index of the medium. i is an integer in interval [1, N-1], where N is the total number of surfaces that can be present, including the calibrated first surface which lies on the balance point of the interferometer and is a free parameter determined by the path difference between the sample and reference arm. l_0 determines the axial resolution of the imaging system. The light source is incident on this sample. The reflection from the ith surface is given by the following relation

$$r_i(t) = a(i) r_s(t - t_i)$$
 (4)

a(i) is a complex number describing reflection from the *i*th surface. The reflection coefficient can be calculated from Fresnel equations [37]. Theoretically, a(i) can have contributions from surfaces other than the *i*th surface. This is due to possible multiple reflections in between the surfaces in the multiple layers

that give the same delay as the ith surface would have produced. But these extra terms can be neglected in biological samples with small refractive index changes because usually r (reflection coefficient) << t (transmission coefficient), which will attenuate the multiple reflections. This approximation was first used in Fizeau interferometer [38] and is often used in interferometry. If the ith surface is absent the a(i) can be considered to be zero. t_i is the time delay corresponding to reflection from the ith surface. Scattering is neglected to keep the formulation simple. The total reflection coming from the object is given by equation

$$r_{\text{total}}\left(t\right) = \sum_{i=1}^{N-1} r_i\left(t\right) \tag{5}$$

The field in the sample arm will be proportional to the $r_{\rm total}$. The proportionality constant depends on 1) the coupling coefficient of the 3db fiber coupler, losses, etc. which are neglected as they correspond to scaling terms, and 2) sample arm length, which is assumed to be equal to that of the reference arm is also neglected.

$$r_{\text{sample}} = r_{\text{total}} = \sum_{i=1}^{N-1} r_i(t)$$
 (6)

The field in the reference arm is the original field of the source that is transmitted to the object and is given by

$$r_{\text{reference}} = r_s(t)$$
 (7)

The complex field at the spectrometer is

$$r(t) = r_s(t) + \sum_{i=1}^{N-1} a(i) r_s(t - t_i)$$
 (8)

To calculate the power spectral density, we will use the Wiener-Khinchin theorem [36] and assume that the statistics of the broadband source is ergodic. The autocorrelation function of this field is given by

$$R(\tau) = \lim_{T \to \infty} \frac{1}{T} \int_{t=-\frac{T}{2}}^{T/2} r(t+\tau) r^*(t) dt$$
 (9)

$$R(\tau) = \lim_{T \to \infty} \frac{1}{T} \int_{t=-\frac{T}{2}}^{T/2} \left[r_s(t+\tau) + \sum_{i=1}^{N-1} a(i) r_s(t-t_i+\tau) \right]$$

$$\times \left[r_s^*(t) + \sum_{i=1}^{N-1} a^*(i) r_s^*(t-t_i) \right] dt$$
 (10)

The interference term is given by

$$R_{\text{intf}}(\tau) = \lim_{T \to \infty} \frac{1}{T} \int_{t=-T/2}^{T/2} \left[\sum_{i=1}^{N-1} a(i) r_s(t - t_i + \tau) r_s^*(t) + \sum_{i=1}^{N-1} a^*(i) r_s(t + \tau) r_s^*(t - t_i) \right] dt$$
(11)

Thus, the interference term of the autocorrelation is given by

$$R_{\text{intf}}(\tau) = \sum_{i=1}^{N-1} a(i) R_s (\tau - t_i) + \sum_{i=1}^{N-1} a^*(i) R_s (\tau + t_i)$$
(12)

Assume a new set of time delay (Supplementary Material S.I) with mapping $t_i \to t_i$ for i > 0, $-t_{-i} \to t_i$ for i < 0, and $t_0 = 0$. Also mapping $a(i) \to \hat{a}(i)$ for i > 0, $a^*(-i) \to \hat{a}(i)$ for i < 0, and $\hat{a}(0) = 0$ represents the calibrated first surface.

$$R_{\text{intf}}(\tau) = \sum_{i=-N+1}^{N-1} \hat{a}(i) R_s(\tau - t_i)$$
 (13)

The effective distance between the 1st and *i*th surface (as defined before) is il_o for i > 0. Performing mapping for time delay t_i as defined above, it can be shown that (14) holds for all possible values of *i* in the interval [-N+1,N-1]

$$t_i = \frac{il_o}{c} \tag{14}$$

Applying Fourier transform on (13)

$$PSD_{\text{intf}}(f) = S(f) \sum_{i=-N+1}^{N-1} \hat{a}(i) \exp\left(\frac{-j2\pi i f l_o}{c}\right) \quad (15)$$

where j is the unit imaginary number. For a spectrometer like a grating spectrometer, we can measure discrete frequencies with resolution f_o . As we have 2N - 1 terms in the summation, we measure the interference term at 2N - 1. For an integer k in [0, 2N - 2]

$$f = k f_0 \tag{16}$$

Usually, the frequency sweep would not start from f = 0, but we ignore an offset term in (16) as it would only contribute to a constant phase term in (15) and can be omitted as a scaling factor. To comply with the Nyquist sampling condition, which is the result of the Nyquist-Shannon sampling theorem [32], the frequency resolution is chosen such that $f_o l_o c^{-1} = (2N-1)^{-1}$ and the spectrometer measures $PSD_{intf}(f)$ at 2N-1 points. If S(f) is known, $\hat{a}(i)$ can be obtained using inverse discrete fourier transform on (15)

$$\hat{a}(i) = \sum_{k=0}^{2N-2} \frac{PSD_{\text{intf}}(kf_o)}{S(kf_o)} \exp\left(\frac{j2\pi}{2N-1}ki\right)$$
 (17)

i for which $\hat{a}(i)$ is non-zero can be used to calculate the optical distance (being il_o), while $\hat{a}(i)$ can be used to calculate the refractive index.

B. Time Delay SD-OCT

In this section, we formulate the working of SD-OCT with a tunable delay line. The result is SD-OCT with an extra modulation term which acts like a filter on the SD-OCT. The transfer function of the filter is in the frequency domain.

We place a tunable delay line in the sample arm as shown in Fig. 1(b) and provide a dispersive delay that can be represented by $\zeta(f)$ in the frequency domain and has a fourier series θ_k with a period (in frequency domain) corresponding to the desired time resolution $t_o = l_o/c$. Thus (8) which is the field at the spectrometer becomes $r(t) = r_s(t)$

$$+\sum_{i=1}^{N-1} a(i) r_s(t-t_i) \otimes \sum_{k=-\infty}^{\infty} \theta_k \delta(t-t_k)$$
 (18)

where \otimes denotes convolution. The field can be written as

$$r(t) = r_s(t) + \sum_{i=1}^{N-1} a(i) \sum_{k=-\infty}^{\infty} \theta_k r_s(t - t_i - t_k)$$
 (19)

Equation (13) is then used to calculate the autocorrelation of the interference term (Supplementary Material S.II)

$$R_{\text{intf}}(\tau) = \sum_{i=-N+1}^{N-1} \hat{a}(i) \sum_{k=-\infty}^{\infty} \theta_k R_s (\tau - t_i - t_k)$$
 (20)

The $PSD_{intf}(f)$ measured at the spectrometer is given by (Supplementary Material S.II)

$$PSD_{\text{intf}}(f) = \left[S(f) \sum_{k=-\infty}^{\infty} \theta_k \exp\left(\frac{-j2\pi k f l_o}{c}\right) \right] \times \sum_{i=-N+1}^{N-1} \hat{a}(i) \exp\left(\frac{-j2\pi i f l_o}{c}\right)$$
(21)

Converting θ_k back to $\zeta(f)$ and discretizing (21) as before

$$PSD_{\text{intf}}(k) = [\zeta(k) S(k)] \sum_{i=-N+1}^{N-1} \hat{a}(i) \exp\left(\frac{-j2\pi}{2N-1}ki\right)$$
(22)

Applying inverse digital fourier transform

$$u\left(n\right) = \mathbb{F}_{D}^{-1} \left\{ \left(2N - 1\right) \frac{PSD_{\inf}(k)}{S\left(k\right)} \right\} \left(n\right) = h\left(n\right) \otimes \hat{a}\left(n\right)$$
(23)

where

$$h(n) = \mathbb{F}_D^{-1} \left\{ \zeta(k) \right\}(n) \tag{24}$$

Thus h(n) acts like a filter on $\hat{a}(n)$. Now taking the Z-transform on both sides

$$U(z_f) = H(z_f) A(z_f)$$
 (25)

The capital letters U, A and H in the above equation are Z-transform, $\mathbb{Z}\{.\}$, of their corresponding small letter and z_f is the complex variable of Z domain as shown in (26). Hence, the use of delay line can be interpreted as a transfer function $H(z_f)$ on $A(z_f)$ in frequency domain.

$$U(z_f) = \mathbb{Z} \{u(n)\}; H(z_f)$$

= $\mathbb{Z} \{h(n)\}; A(z_f) = \mathbb{Z} \{\hat{a}(n)\}$ (26)

C. Cross-Phase Modulation SD-OCT

In this section, we formulate the working of SD-OCT with two phase modulators. The result here is again SD-OCT with an extra modulation term but with transfer function in the time domain.

We place the two phase modulator, one in the sample arm and the other in the reference arm as shown in Fig. 1(c). The field in the sample arm is modulated by $\phi_1(t)$ while the field in the reference arm is modulated by $\phi_2(t)$. Thus, the field at the spectrometer is given by

$$r(t) = r_s(t) \exp(j\phi_2(t)) + \sum_{i=1}^{N-1} a(i) r_s(t - t_i) \exp(j\phi_1(t))$$
 (27)

The field in this case is no longer ergodic (not even wide sense stationary). To determine the power spectral density at the spectrometer, we will rederive Wiener-Khinchin Theorem as direct autocorrelation is unable to provide the power spectral density. Let U_T be the Fourier transform r(t) windowed in a region of length T with center at t=0.

$$U_T(f) = \int_{-T/2}^{T/2} r(t) \exp(-j2\pi f t) dt$$
 (28)

Then the power spectral density is given by

$$PSD(f) = \lim_{T \to \infty} \frac{1}{T} E\left[\left| U_T(f) \right|^2 \right]$$
 (29)

where E[.] is the expected value of the statistics.

$$PSD(f) = \lim_{T \to \infty} \frac{1}{T} E \left[\int_{t=-\frac{T}{2}}^{\frac{T}{2}} r(t) \exp(-2\pi f t) dt \right]$$

$$\times \int_{t'=-T/2}^{T/2} r^*(t) \exp(-2\pi f t') dt'$$
(30)

The interference term is given by

 PSD_{intf} (f)

$$= \lim_{T \to \infty} \frac{1}{T} E \left[\int_{t=-T/2}^{T/2} \int_{t'=-T/2}^{T/2} \left[\sum_{i=1}^{N-1} a\left(i\right) r_s\left(t-t_i\right) r_s^*\left(t'\right) \right. \right.$$

 $\times \exp\left(j\phi_1\left(t\right) - j\phi_2\left(t\right)\right)$

$$+ \sum_{i=1}^{N-1} a^{*}(i) r_{s}^{*}(t-t_{i}) r_{s}(t') \times \exp(j\phi_{2}(t) - j\phi_{1}(t))$$

$$\exp\left(-j2\pi f\left(t-t'\right)\right) dt dt'$$
(31)

 $PSD_{intf}(f)$

$$= \lim_{T \to \infty} \frac{1}{T} \int_{t=-T/2}^{T/2} \int_{t'=-T/2}^{T/2}$$

$$\times \left[\sum_{i=1}^{N-1} a(i) E \left[r_s (t - t_i) r_s^* (t') \right] \right]$$

$$\times \exp(j\phi_{1}(t) - j\phi_{2}(t)) + \sum_{i=1}^{N-1} a^{*}(i) E[r_{s}^{*}(t - t_{i}) r_{s}(t')] \times \exp(j\phi_{2}(t) - j\phi_{1}(t))$$

$$\exp(-j2\pi f(t - t')) dt dt'$$
(32)

As $r_s(t)$ is an ergodic process, the expected value in the above equation is the autocorrelation function as defined by (2)

$$PSD_{\text{intf}} (f)$$

$$= \lim_{T \to \infty} \frac{1}{T} \int_{t=-T/2}^{T/2} \int_{t'=-T/2}^{T/2} \left[\sum_{i=1}^{N-1} a(i) R_s (t - t' - t_i) \right] \times \exp(j\phi_1(t) - j\phi_2(t))$$

$$+ \sum_{i=1}^{N-1} a^* (i) R_s (t - t' + t_i) \times \exp(j\phi_2(t) - j\phi_1(t)) \right]$$

$$\exp(-j2\pi f (t - t')) dt dt'$$
(33)

Substituting $t = t' + \tau$ and changing limits accordingly

$$PSD_{intf}(f)$$

$$= \sum_{i=1}^{N-1} a(i) \lim_{T \to \infty} \frac{1}{T} \int_{\tau=-T}^{T} R_s(\tau - t_i)$$

$$\times \int_{t'=-T/2-\tau}^{T/2-\tau} \exp(j\phi_1(t'+\tau) - j\phi_2(t') - 2j\pi f\tau) dt' d\tau$$

$$+ \sum_{i=1}^{N-1} a^*(i) \lim_{T \to \infty} \frac{1}{T} \int_{\tau=-T}^{T} R_s(\tau + t_i)$$

$$\times \int_{t'=-T/2-\tau}^{T/2-\tau} \exp(j\phi_2(t'+\tau) - j\phi_1(t') - 2j\pi f\tau) dt' d\tau$$
(34)

The second integral in the limit in both the summation terms becomes a cross-correlation function.

$$PSD_{\text{intf}}(f)$$

$$= \sum_{i=1}^{N-1} a(i) \int_{-\infty}^{\infty} R_s(\tau - t_i) R_{\phi}(\tau) \exp(-j2\pi f \tau) d\tau$$

$$+ \sum_{i=1}^{N-1} a^*(i) \int_{-\infty}^{\infty} R_s(\tau + t_i) R_{\phi}^*(-\tau) \exp(-j2\pi f \tau) d\tau$$
(35)

where,

$$R_{\phi} (\tau) = \lim_{T \to \infty} \frac{1}{T} \int_{t = -T/2}^{T/2} \exp(j\phi_1(t + \tau) - j\phi_1(t))$$
(36)

The remaining integral in (34) resembles fourier transformation. Mapping a(i) to $\hat{a}(i)$ as before

$$PSD_{\mathrm{intf}}\ \left(f\right) = \left[S\left(f\right)\sum_{i=1}^{N-1}\hat{a}\left(i\right)\exp\left(-j2\pi ft_{i}\right)\right]\ \otimes\Phi\left(f\right)$$

$$+\left[S\left(f\right)\sum_{i=1}^{N-1}\hat{a}^{*}\left(i\right)\exp\left(-j2\pi ft_{i}\right)\right]\otimes\Phi^{*}\left(f\right)\tag{37}$$

where.

$$\Phi (f) = \mathbb{F} \left\{ R_{\phi} (\tau) \right\} (f) \tag{38}$$

The second term in (35) is the negative part of information in length domain. If support of $\Phi^*(f)$, which acts as filter, is small compared to N, the second summation can be ignored in the post-processing of first summation which contains all information of a(i). Thus, for the first term, the applied phase modulation results in a convolution in the frequency domain with transfer function $R_{\phi}(\tau)$. Discretizing the interference term and converting to Z domain gives

$$U(z_t) = H(z_t) A(z_t)$$

$$U(z_t) = \mathbb{Z} \left\{ PSD_{\text{intf}}(k) \right\};$$

$$A(z_t) = \mathbb{Z} \left\{ S(k) \sum_{i=1}^{N-1} \hat{a}(i) \exp(-j2\pi f t_i) \right\};$$

$$H(z_t) = \mathbb{Z} \left\{ \Phi(k) \right\}$$

$$(40)$$

Equation (39) represents a linear system with transfer function in time domain. The Z-transforms can be calculated by (40). Hence, phase modulation gives transfer function in the length domain unlike the delay line in (25) that results in transfer function in the frequency domain.

D. Multirate Filter Bank

In the previous sections, we showed that the use of delay line/phase modulators result in transfer function in frequency/time domain respectively. In this section, we use these transfer functions to set up a multirate filter bank scheme as shown in Fig. 2. The left hand of Fig. 2 is the SD-OCT where the transfer functions are implemented as discussed in previous sections. The right hand side of Fig. 2 is implemented digitally after detection on a spectrometer. We show that this scheme can improve resolution in the time/frequency domain respectively.

Use of a tunable delay line in represent a linear system in which multirate signal processing can be used to increase the length resolution of the system as shown in Fig. 2. Equation (25) corresponds to a transfer function block with the Z-transform in the frequency domain. As the maximum bandwidth of the spectrometer is usually limited, it may cause the resolution in the length domain (axial resolution) to be less than desired, resulting in under-sampling. Hence phase modulation can be interpreted as a transfer function [H(z)] on the resolution limited signal [A(z)]. Consequently, (25) corresponds to a single channel on the left hand side of Fig. 2. Likewise, multiple scans can be used to obtain information for all the channels. Next, the channels on the right-hand side are implemented on a digital computer. The depth information can be retrieved numerically by implementing the synthesis filters [F(z)] and then combining the various channels. Similarly, for cross-arm phase modulation, (39) corresponds to a single channel but here the Z domain represents time domain. If the resolution of spectrometer is limited, multiple

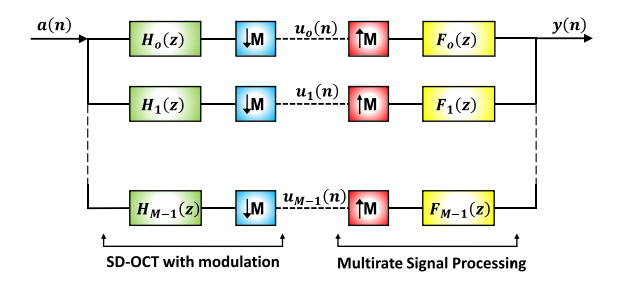


Fig. 2. Representation of SD-OCT and the signal processing in form of a block diagram. The Z domain corresponds to the frequency or length domain with respect to the implementation of delay line or cross-phase modulation. a(n) represents the optical signal that the interference term of SD-OCT carries and our aim is to recover this signal digitally. The green blocks represent analysis filters that are provided optically using a delay line or phase modulators. The blue blocks with downwards arrow represent downsampling which is naturally present in the system when the spectrometer has worse bandwidths or resolution than desired. Broken lines represent spectrum measurement using a spectrometer. The red blocks with upwards arrow represent upsampling which is implemented on a digital computer. The vellow blocks represent synthesis filters that can be calculated from the theory of multirate signal processing and are also implemented digitally. Such scans are made M times with different filters as shown as M different channels. Finally, all the channels are combined to give y(n) which should be close to a perfect reconstruction of a(n) with desire resolution/maximum unambiguous range.

scans can be used to obtain a spectrum of desired resolution and thus providing the desired maximum depth of the OCT. In the multirate scheme with two channels, for doubling the resolution, two different A scans need to be performed at the same position in the transverse direction. Hence, the speed of acquiring B scan image will be halved. Similarly, the speed of B scan will decrease as the number of channels increases. Reducing the speed of the B scan should be feasible for biological samples as the structure of biological samples for OCT application do not usually change over time.

Let the spectrometer have a bandwidth that is M times smaller than required so that the axial resolution is downsampled by a factor of M from the desired l_o . This can be depicted by the block diagram as shown in Fig. 2. The block diagram resembles a single channel of the M channel filter bank. If we make the measurement M times with M different analysis filters (H_m) , the ideally sampled signal can be reconstructed using synthesis filters (F_m) . For demonstration purposes, we discuss the situation when M=2 and thus m=[0,1]. The perfect reconstruction (PR) of a(n), which is the ideally sampled signal, is said to be achieved when y(n)=a(n-K), i.e., y(n) is a perfect replica of a(n) and is with a shift of K points. This removes both aliasing and distortion from the reconstruction. For a two-channel filter bank, the PR condition is given by

$$\begin{bmatrix} F_o\left(z\right) \\ F_1\left(z\right) \end{bmatrix} = \frac{2z^{-L}}{\Delta\left(z\right)} \begin{bmatrix} H_1\left(-z\right) \\ -H_o\left(-z\right) \end{bmatrix} \tag{41}$$

where L = 2K + 1 and $\Delta(z)$ is given by

$$\Delta(z) = H_o(z) H_1(-z) - H_o(-z) H_1(z)$$
 (42)

Similarly, the spectrometer can have resolution M time worse than required so the frequency resolution is downsampled by M. Hence, the block diagram can be again applicable to this case but with inverted domains. Analysis filter $H_m(z)$ can be calculated

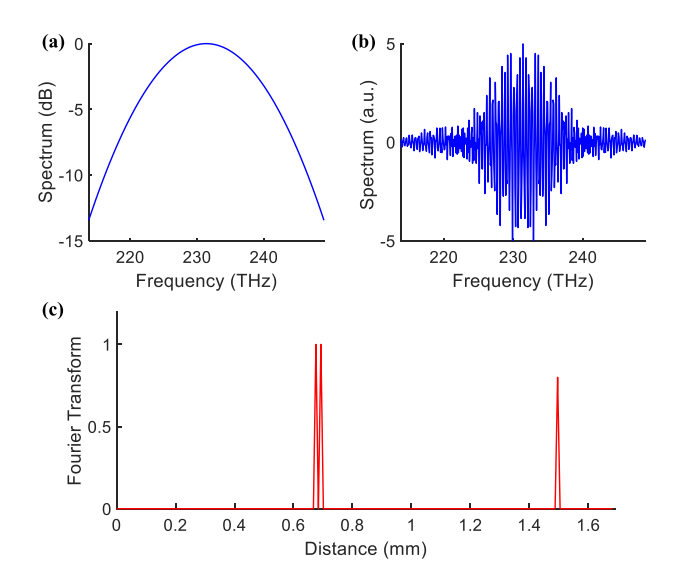


Fig. 3. Demonstration of SD-OCT (a) Spectrum of the broadband source used for SD-OCT. (b) Spectrum detected by the spectrometer. (c) Inverse fourier transform of the detected spectrum that can be used to locate the surfaces and their thickness in the object.

using (26) and (40) depending on the tunable delay line/phase modulation given and synthesis filter $F_m(z)$ can be calculated using (41) and (42).

We stress that although (26) and (39) look the same for both the delay line and cross-arm phase modulation scenarios, it is important to know that their domain is opposite (specifically frequency and length respectively). By performing multiple scans, axial resolution can be improved in the delay line case while the maximum depth is increased in the cross arm phase modulation. Consequently, the delay is of interest when it is desired to overcome the limitation of the bandwidth of the spectrometer, while the cross-arm phase modulation is of interest when it is desired to overcome the frequency resolution limit of the system. Conceptually, these two cases are equivalent to the presence of a downsampled block in the system. Analysis filters are implemented optically using delay line/phase modulators while the synthesis filters and upsampling blocks are implemented on a digital computer. As the number of channels possible can only be integers, the resolution/maximum unambiguous range can only be improved by an integral multiple.

III. SIMULATION RESULTS

First, to demonstrate the working of a regular SD-OCT, we simulate a single A-scan in this section. We assume a source that has a Gaussian shape and is centered around 1300 nm wavelength as shown in Fig. 3(a). The spectrometer used is assumed to have a bandwidth of 200 nm and 0.5 nm resolution. This corresponds to an axial optical resolution of 8.45 μ m and maximum optical depth of 1.7 mm. Consider a simple object that is under investigation and is made up of three reflective surfaces. Two of them are at about optical distance of 0.69 mm with distance between them being 16.9 μ m. The third surface is present at a distance of 1.5 mm. The interference spectrum that is detected at the spectrometer is given by Fig. 3(b). Computing

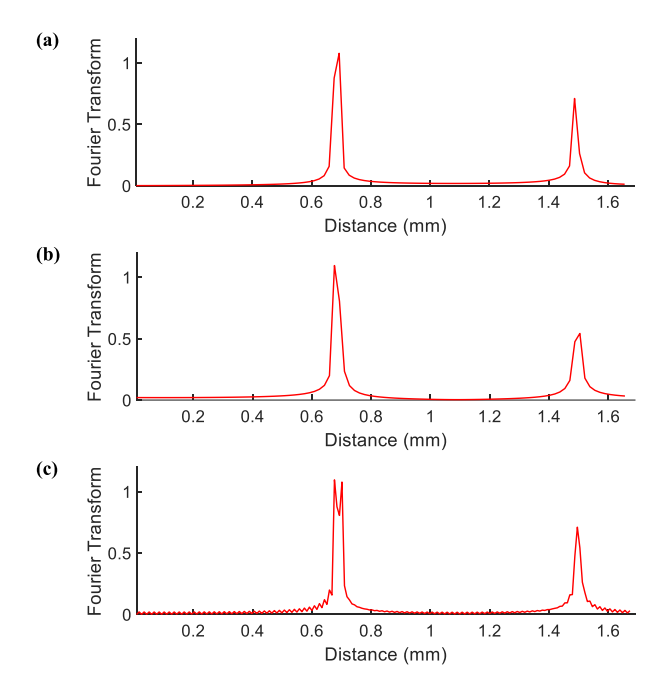


Fig. 4. Demonstration of SD-OCT with delay line to improve axial resolution (a) measured depth information from first channel. The limited bandwidth of spectrometer leads to less than desired axial resolution. Thus, the surface close together cannot be distinguished as peaks. (b) Measurement from the second channel that utilizes a delay line in the sample arm. (c) Combined graph from both the channels is able to resolve the surface close together and the position of all three surfaces are known with 2 times the accuracy compared to a single channel.

the inverse fourier transform gives the location of these surfaces in the form of peaks as shown in Fig. 3(c).

Now, we assume that the bandwidth of the spectrometer is limited to 100 nm, i.e., from 1200 nm to 1300 nm. This would mean that resolution of SD-OCT is 16.9 μ m, and for the same object described above, the first two surfaces are not resolvable by the SD-OCT. This is shown in Fig. 4(a) where only one peak is visible for the first two surfaces. This measurement acts like our first channel where no delay is present in the sample arm (Supplementary Material S.III). Next, for a second channel we provide a delay given by:

$$\zeta(f) = \exp(i2\pi f t_0) \tag{43}$$

where $t_o = 28.3$ fs. The delay chosen here corresponds to half of length resolution and provides a single delay in the z_f domain. The length domain information of the second channel is shown by Fig. 4(b). Thus, for these two channels

$$H_o(z_f) = 1; H_1(z_f) = z_f^{-1}$$
 (44)

To fulfill the PR condition, the parameters for reconstruction can be calculated as follows

$$F_o(z_f) = z_f^{-1}; F_1(z_f) = 1;$$

 $\Delta(z_f) = -2z_f^{-1}; K = 1.$ (45)

Using both the channels and the synthesis filters, the depth information of the SD-OCT can be computed with 2 times better

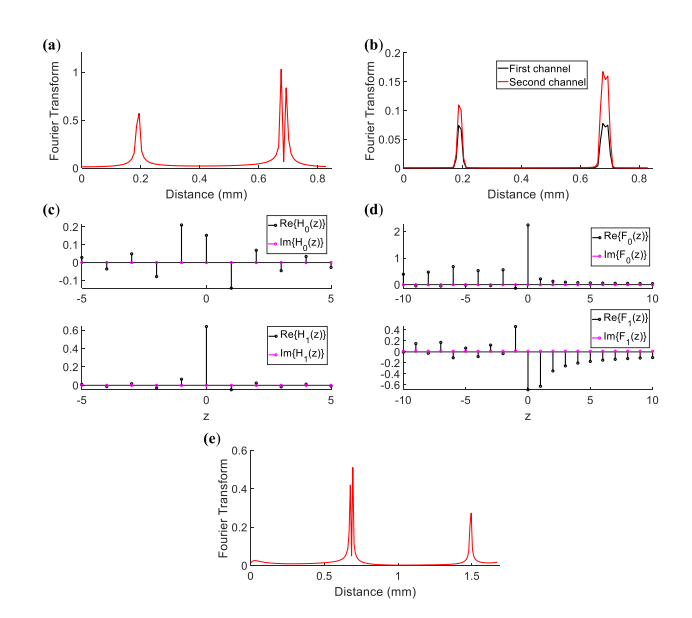


Fig. 5. Demonstration of SD-OCT with phase modulation to improve maximum ambiguous depth (a) measured depth information using a limited resolution spectrometer. The less than desired resolution results in aliasing and the location of third peak is not its true position. (b) The analysis filters implemented using phase modulation. (c) Measured depth information in the two channels after implementing phase modulation. (d) The synthesis filter calculated numerically using filter bank theory. (e) Reconstructed signal by combining the two channels after implementing synthesis filters. The maximum unambiguous range has doubled, and the measured position of the third peak is its true position.

resolution than just a single channel. Also, the two surfaces can be resolved as the resolution has improved to distinguish their peaks. The result from combined channel is shown in Fig. 4(c).

Next, we consider the case when the resolution of the spectrometer is limited to 1 nm. This results in a maximum depth of 0.85 mm and the second peak lies beyond the maximum unambiguous range. Thus, when making measurement using this limited resolution system, the aliased version of third peak appears which is not the true position of this peak. This is shown Fig. 5(a) where the peak that should be at 1.5 mm appears around 0.2 mm. To increase the maximum depth of the OCT and obtain the true position of the third peak (and also the first two peaks) we use two different channels with different phase modulation. For first channel we use $\phi_{11}(t)$ and $\phi_{12}(t)$, while for the second channel we use $\phi_{21}(t)$ and $\phi_{22}(t)$. The optical phase modulation is usually generated using RF electrical signals. As arbitrary signals are difficult and cost-ineffective at high speed, we assume sinusoidal modulations. Thus, the phase modulation can be given by:

$$\phi_{pq}(t) = A_p \sin(2\pi f_{pq}t) \tag{46}$$

where $p,q\in[1,2]$. We choose the following values for the demonstration: $f_{11}=f_{21}=22.1~\mathrm{GHz}$; $f_{12}=f_{22}=44.2~\mathrm{GHz}$; $A_1=2~\mathrm{rad}$; $A_2=1~\mathrm{rad}$. The two analysis filters can be calculated by using (36), (39) and (40), and are shown in Fig. 5(b). After the analysis filters are implemented via phase modulation, the signal is detected using spectrometer and are shown in Fig. 5(c). The signal is then upsampled by a factor of 2 in frequency domain. The synthesis filters can be calculated using (41) and be implemented digitally on the upsampled

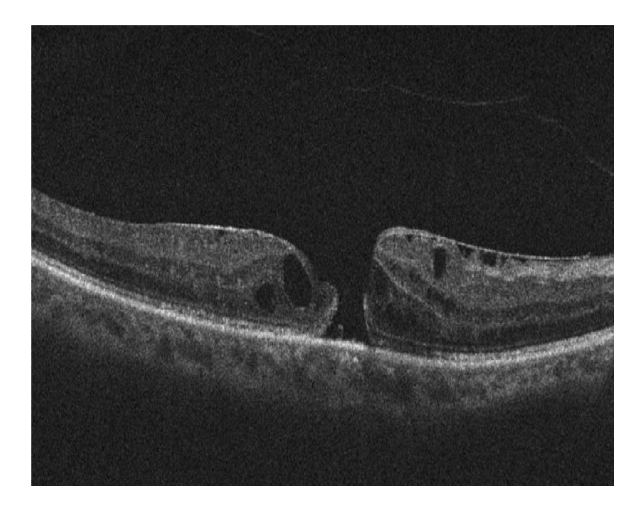


Fig. 6. Experimental image of a macular hole in retina used for simulation of a two channel multirate SD-OCT.

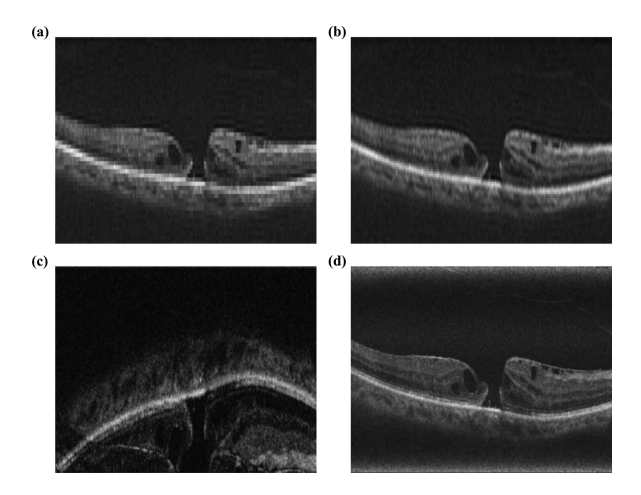


Fig. 7. Implementation of multirate SD-OCT on the image of macular hole in retina. (a) Simulated low resolution image which will result from limited bandwidth of the spectrometer. (b) Image after implementing two channel filter bank with delay line configuration on (a). The axial resolution is improved by a factor of 2. (c) Simulated image when the resolution of spectrometer is half of the original. (d) Image after implementation of two channel filter bank in phase modulator configuration on (c). As the maximum unambiguous range has been doubled, the true positions of all the surfaces are visible.

signal. Note that to implement the synthesis filters $\Delta(z_t)$ should be invertible. This can be ensured by either converting $\Delta(z_t)$ to minimum phase filter or engineering stable synthesis filters using various modulation schemes. The coefficients of the synthesis filter are shown in Fig. 5(d). After implementing the synthesis filters, the channels are combined to develop the depth information with double the maximum ambiguous length. As shown in Fig. 5(e) the true position of the third surface is recovered without any aliasing.

We validate the multirate SD-OCT on experimental data and simulate a two channel filter bank to improve axial resolution/range by a factor of two. For this purpose, we use an image of macular hole in retina which is a part of Optical Coherence Tomography Retinal Dataset [39]. The original image used for this simulation is shown in Fig. 6. The original image acts like an experimental object on which multirate SD-OCT is simulated.

We simulate the image in Fig. 7(a) which corresponds to a scenario where the bandwidth of spectrometer is limited and reduces the axial resolution of the image. To improve the axial resolution by a factor of 2, we simulate a multirate SD-OCT with a delay line. We use the filters in (43)–(45) to set up the two channels filter bank. The image after passing through the multirate filter bank is shown in Fig. 7(b). The new image has twice the axial resolution compared Fig. 7(a). Then, we simulate the image in Fig. 7(c) which corresponds to a scenario where the resolution of the spectrometer is half of the original. This leads to aliasing of surfaces that are beyond the maximum unambiguous range and the surfaces overlap. We simulate a multirate SD-OCT with phase modulators. The same modulation and filters, as shown in (46), Fig. 5(c) and (d), are used for the two channel filter bank. The resulting image is shown in Fig. 7(d). The maximum unambiguous range has been doubled and the true positions of all the surfaces appear.

IV. CONCLUSION

In summary, the multirate SD-OCT was formulated and validated with simulation. In this work, a 2 channel system is simulated, but in theory, a higher number of channels can be used to form a more complex multirate filter bank [40]. Generally, to determine the synthesis filters for both domains, the analysis filter matrix [40] needs to be inverted. This places a constraint on the analysis filters to have an invertible matrix. Also, the analysis filters will be limited by the speed and shape of modulation that can be given via delay line/phase modulators. Hence, considering both mathematical and hardware constraints, the delays and frequency of modulation are chosen; and the analysis filters are engineered. This also applies for M > 2 channels. For standard SD-OCT, signal-to-noise ratio will have contributions from various components used in the system such as the source and the spectrometer. The signal-to-noise ratio for both multirate SD-OCT implementations will depend on the type of filter used and its implementation. The synthesis filter calculated from the (41) and (42) can have infinite support and would be approximated by a filter of finite support to perform the digital part of the multirate filter bank. The process of truncation and then converting the filter to minimum phase will bring in some imperfections to the reconstruction. Also, the limited bandwidth inherently adds sinc function to the reconstructed signal which will contribute to the noise. For single A-scan simulation, no artificial noise is given to the ideal sample. The noise added due to the above reasons give peak SNR of 18.18 dB and 22.92 dB for increasing resolution and range respectively. For improving the axial resolution, the accuracy of the optical system that is applicable for a single scan will also hold for multiple channels as long as the object and system are stable and have little drift. This is an acceptable assumption for biological samples whose position and property will not change significantly in between consecutive scans. For improving the maximum range, the extra requirement compared to a single scan is enough SNR from depths further than the Nyquist limit should be available. Also, the optical components in front of object should be able to collect this signal.

In recent literature, a number of techniques have been developed to improve the OCT either using superior hardware [41], [42] or complex post-processing [43], [44]. The novelty of our multirate SD-OCT is not only that it combines the effect of both additional hardware and post processing but also is compatible with some of the other existing technique as use of filters and multiple channels is universally applicable to a linear system. Also, some of the techniques previously shown in literature such as use of multiple broadband sources [30] to improve axial resolution is a special case of multirate SD-OCT where each broadband source can be considered as separate channel multiplexed in wavelength rather in time as in our case.

The resolution and bandwidth of the SD-OCT system are often limited by the spectrometer. Grating spectrometers are widely used in SD-OCT [45] and its performance is determined by various physical parameters such as grating length, number of gratings, material used, wavelengths, etc. [46]. Often these parameters are interdependent and are restricted by technology and feasibility. This, in turn, makes the resolution and bandwidth of the spectrometer interdependent and limited. By using multirate SD-OCT, not only the cost of spectrometer is reduced for one of bandwidth and resolution, but it also gives the opportunity sacrifice one for the other as the sacrificed parameter can be improved by this technique. The price to pay for this technique is the modulator/delay line cost and the extra time required to carry out multiple scans. As the object in SD-OCT are usually stationary, extra scans would not pose a challenge.

ACKNOWLEDGMENT

The authors would like to acknowledge Alexander Franzen for providing ComponentLibrary.

REFERENCES

- [1] D. Huang et al., "Optical coherence tomography," *Science*, vol. 254, no. 5035, pp. 1178–1181, 1991, doi: 10.1126/science.1957169.
- [2] A. F. Fercher, K. Mengedoht, and W. Werner, "Eye-length measurement by interferometry with partially coherent light," *Opt. Lett.*, vol. 13, pp. 186–188, 1988.
- [3] R. Leitgeb, C. K. Hitzenberger, and A. F. Fercher, "Performance of Fourier domain vs. time domain optical coherence tomography," *Opt. Exp.*, vol. 11, pp. 889–894, 2003.
- [4] J. S. Schuman, "Spectral domain optical coherence tomography for glaucoma (an AOS thesis)," *Trans. Amer. Ophthalmological Soc.*, vol. 106, pp. 426–458, 2008.
- [5] O. Shalabi et al., "Swept-source optical coherence tomography changes and visual acuity among Palestinian retinitis Pigmentosa patients: A crosssectional study," *BMC Ophthalmol.*, vol. 21, no. 1, Jul. 2021, Art. no. 289, doi: 10.1186/s12886-021-02047-6.
- [6] L. Lim, G. Cheung, and S. Lee, "Comparison of spectral domain and swept-source optical coherence tomography in pathological myopia," *Eye*, vol. 28, pp. 488–449, 2014, doi: 10.1038/eye.2013.308.
- [7] A. R. Miller et al., "Comparison between spectral-domain and swept-source optical coherence tomography angiographic imaging of choroidal neovascularization," *Invest. Ophthalmol. Vis. Sci.*, vol. 58, no. 3, pp. 1499–1505, 2017, doi: 10.1167/iovs.16-20969.
- [8] B. Tan et al., "Comparison of a commercial spectral-domain OCT and swept-source OCT based on an angiography scan for measuring circumpapillary retinal nerve fibre layer thickness," *Brit. J. Ophthalmol.*, vol. 104, no. 7, pp. 974–979, 2020, doi: 10.1136/bjophthalmol-2019-314706.
- [9] J. Men et al., "Optical coherence tomography for brain imaging and developmental biology," *IEEE J. Sel. Topics Quantum Electron.*, vol. 22, no. 4, pp. 120–132, Jul./Aug. 2016, doi: 10.1109/JSTQE.2015.2513667.

- [10] C. Y. Cheung, M. K. Ikram, C. Chen, and T. Y. Wong, "Imaging retina to study dementia and stroke," *Prog. Retinal Eye Res.*, vol. 57, pp. 89–107, 2017, doi: 10.1016/j.preteyeres.2017.01.001.
- [11] Z. Tang et al., "Assessment of retinal neurodegeneration with spectral-domain optical coherence tomography: A systematic review and meta-analysis," *Eye (London, England)*, vol. 35, no. 5, pp. 1317–1325, 2021, doi: 10.1038/s41433-020-1020-z.
- [12] M. Bhende, S. S. Muna, M. K. Parthasarathy, and S. Ramya, "Optical coherence tomography: A guide to interpretation of common macular diseases," *Indian J. Ophthalmol.*, vol. 66, no. 1, pp. 20–35, 2018, doi: 10.4103/ijo.IJO_902_17.
- [13] X. Yao, Y. Gan, E. Chang, H. Hibshoosh, S. Feldman, and C. Hendon, "Visualization and tissue classification of human breast cancer images using ultrahigh-resolution OCT," *Lasers Surg. Med.*, vol. 49, pp. 258–269, 2017, doi: 10.1002/lsm.22654.
- [14] B. Konkel et al., "Fully automated analysis of OCT imaging of human kidneys for prediction of post-transplant function," *Biomed. Opt. Exp.*, vol. 10, no. 4, pp. 1794–1821, Mar. 2019, doi: 10.1364/BOE.10.001794.
- [15] R. K. Prakasam et al., "Spectral-domain optical coherence tomography for determination of retinal thickness in pediatric patients with mild-tomoderate chronic kidney disease: A cross-sectional study," *Curr. Eye Res.*, vol. 44, no. 2, pp. 206–211, 2019, doi: 10.1080/02713683.2018.1522649.
- [16] M. Szczepanik et al., "The use of optical coherence tomography for skin evaluation in healthy rats," *Vet. Dermatol.*, vol. 33, no. 4, 2022, Art. no. 296e69, doi: 10.1111/vde.13071.
- [17] B. Lee et al., "High-speed, ultrahigh-resolution spectral-domain OCT with extended imaging range using reference arm length matching," *Transl. Vis. Sci. Technol.*, vol. 9, no. 7, Jun. 2020, Art. no. 12, doi: 10.1167/tvst.9.7.12.
- [18] L. Bernstein et al., "Ultrahigh resolution spectral-domain optical coherence tomography using the 1000-1600 nm spectral band," *Biomed. Opt. Exp.*, vol. 13, no. 4, pp. 1939–1947, Mar. 2022, doi: 10.1364/BOE.443654.
- [19] Y. Matsui, M. Kondo, E. Uchiyama, R. Mityata, and H. Matsubara, "New clinical ultrahigh-resolution SD-OCT using A-scan matching algorithm," *Graefe's Arch. Clin. Exp. Ophthalmol.*, vol. 257, pp. 255–263, 2019, doi: 10.1007/s00417-018-4183-6.
- [20] M. Hangai, M. Yamamoto, A. Sakamoto, and N. Yoshimura, "Ultrahigh-resolution versus speckle noise-reduction in spectral-domain optical co-herence tomography," *Opt. Exp.*, vol. 17, no. 5, pp. 4221–4235, 2019, doi: 10.1364/oe.17.004221.
- [21] R. F. Spaide, H. Koizumi, and M. C. Pozonni, "Enhanced depth imaging spectral-domain optical coherence tomography," *Amer. J. Ophthalmol.*, vol. 146, no. 4, pp. 496–500, 2008, doi: 10.1016/j.ajo.2008.05.032.
- [22] A. Sakamoto, M. Hangai, and N. Yoshimura, "Spectral-domain optical coherence tomography with multiple B-scan averaging for enhanced imaging of retinal diseases," *Ophthalmology*, vol. 115, no. 6, pp. 1071–1078.e7, 2008, doi: 10.1016/j.ophtha.2007.09.001.
- [23] T. Bajraszewski, M. Wojtkowski, M. Szkulmowski, A. Szkulmowska, R. Huber, and A. Kowalczyk, "Improved spectral optical coherence tomography using optical frequency comb," *Opt. Exp.*, vol. 16, pp. 4163–4176, 2008, doi: 10.1364/OE.16.004163.
- [24] R. A. Leitgeb, C. K. Hitzenberger, A. F. Fercher, and T. Bajraszewski, "Phase-shifting algorithm to achieve high-speed long-depth-range probing by frequency-domain optical coherence tomography," *Opt. Lett.*, vol. 28, pp. 2201–2203, 2003, doi: 10.1364/OL.28.002201.
- [25] Y. Takahashi, Y. Watanabe, and M. Sato, "Application of the maximum entropy method to spectral-domain optical coherence tomography for enhancing axial resolution," *Appl. Opt.*, vol. 46, pp. 5228–5236, 2007, doi: 10.1364/AO.46.005228.
- [26] S. S. Lee, W. Song, and E. S. Choi, "Spectral domain optical coherence tomography imaging performance improvement based on field curvature aberration-corrected spectrometer," *Appl. Sci.*, vol. 10, 2020, Art. no. 3657, doi: 10.3390/app10103657.
- [27] P. J. Marchand et al., "Soliton microcomb based spectral domain optical coherence tomography," *Nature Commun.*, vol. 12, 2021, Art. no. 427, doi: 10.1038/s41467-020-20404-9.
- [28] E. Bo, X. Liu, S. Chen, X. Yu, X. Wang, and L. Liu, "Spectral-domain optical coherence tomography with dual-balanced detection for autocorrelation artifacts reduction," *Opt. Exp.*, vol. 23, pp. 28050–28058, 2015, doi: 10.1364/OE.23.028050.
- [29] H. Kim, P. U. Kim, M. G. Hyeon, Y. Choi, J. Kim, and B. Kim, "High-resolution, dual-depth spectral-domain optical coherence tomography with interlaced detection for whole-eye imaging," *Appl. Opt.*, vol. 55, pp. 7212–7217, 2016, doi: 10.1364/AO.55.007212.
- [30] H. Wang, M. W. Jenkins, and A. M. Rollins, "A combined multiple-SLED broadband light source at 1300 nm for high resolution optical coherence tomography," *Opt. Commun.*, vol. 281, no. 7, pp. 1896–1900, 2008, doi: 10.1016/j.optcom.2007.08.073.

- [31] J. F. de Boer, B. Cense, B. Hyle Park, M. C. Pierce, G. J. Tearney, and B. E. Bouma, "Improved signal-to-noise ratio in spectral-domain compared with time-domain optical coherence tomography," *Opt. Lett.*, vol. 28, pp. 2067–2069, 2003, doi: 10.1364/OL.28.002067.
- [32] C. E. Shannon, "Communication in the presence of noise," *Proc. IRE*, vol. 37, no. 1, pp. 10–21, 1949, doi: 10.1109/JRPROC.1949. 232969.
- [33] M. A. Vetterli, "A theory of multirate filter banks," *IEEE Trans. Acoust., Speech, Signal Process.*, vol. 35, no. 3, pp. 356–372, Mar. 1987, doi: 10.1109/JRPROC.1949.232969.
- [34] R. Kumar, A. Kumar, and S. P. Singh, "A review on decade of multirate filters," in *Proc. 2nd Int. Conf. Electron. Commun. Syst.*, 2015, pp. 1615–1620, doi: 10.1109/ECS.2015.7124859.
- [35] P. Gaur, A. Grieco, N. Alshamrani, D. Almutairi, and Y. Fainman, "Universal photonics tomography," *Opt. Exp.*, vol. 30, pp. 19222–19235, 2022, doi: 10.1364/OE.454497.
- [36] J. W. Goodman, Statistical Optics. Hoboken, NJ, USA: Wiley, 1985.
- [37] P. Gupta, A. Pandey, K. Vairagi, and S. K. Mondal, "Solving Fresnel equation for refractive index using reflected optical power obtained from Bessel beam interferometry," *Rev. Sci. Instrum.*, vol. 90, no. 1, 2019, Art. no. 015110, doi: 10.1063/1.5043240.
- [38] C. Han, H. Ding, B. Li, L. Shi, and H. Xu, "Miniature Fourier transform spectrometer based on a fiber-tip interferometer," *Opt. Exp.*, vol. 30, pp. 15134–15148, 2022, doi: 10.1364/OE.456320.

- [39] P. Gholami and V. Lakshminarayanan, Optical Coherence Tomography Image Retinal Database. Ann Arbor, MI, USA: Inter-University Consortium for Political and Social Research [distributor], 2019, doi: 10.3886/E108503V1.
- [40] G. Strang and T. Nguyen, Wavelets and Filter Banks. Philadelphia, PA, USA: SIAM, 1996.
- [41] D. S. Shreesha Rao et al., "Shot-noise limited, supercontinuum-based optical coherence tomography," *Light Sci. Appl.*, vol. 10, 2021, Art. no. 133, doi: 10.1038/s41377-021-00574-x.
- [42] L. Wang and L. Liu, "Corneal imaging with extended imaging range using dual spectrometer high-resolution SD-OCT," in *Proc. Conf. Lasers Electro-Opt.*, 2019, Paper JTu2A.6.
- [43] X. Liu and J. K. Kang, "Compressive SD-OCT: The application of compressed sensing in spectral domain optical coherence tomography," *Opt. Exp.*, vol. 18, pp. 22010–22019, 2010, doi: 10.1364/OE.18.022010.
- [44] M. Zhang et al., "Advanced image processing for optical coherence tomographic angiography of macular diseases," *Biomed. Opt. Exp.*, vol. 6, pp. 4661–4675, 2015, doi: 10.1364/BOE.6.004661.
- [45] S. Samadi, J. Dargahi, and S. Narayanswamy, "Design and optimization of a linear wavenumber spectrometer with cylindrical optics for line scanning optical coherence tomography," *Sensors*, vol. 21, no. 19, 2021, Art. no. 6463, doi: 10.3390/s21196463.
- [46] F. Kneubühl, "Diffraction grating spectroscopy," Appl. Opt., vol. 8, pp. 505–519, 1969, doi: 10.1364/AO.8.000505.